SUPPORTING INFORMATION

Chemically driven magnetic responsivity to multiple physical stimuli in a spin-crossover layered iron(II)-rhenium(V) framework

Tomasz Charytanowicz,[ab] Michał Heczko,[a] Katarzyna Dziedzic-Kocurek,[c] Dawid Pinkowicz,[a] Shin-ichi Ohkoshi,[d] Szymon Chorazy,*[a] and Barbara Sieklucka*[a]

[a]Faculty of Chemistry, Jagiellonian University, Gronostajowa 2, 30-387 Kraków, Poland. [b]Doctoral School of Exact and Natural Sciences, Jagiellonian University in Kraków Łojasiewicza 11, 30-348 Kraków, Poland. [c]Marian Smoluchowski Institute of Physics, Jagiellonian University, Łojasiewicza 11, 30-348 Kraków, Poland. [d]Department of Chemistry, School of Science, The University of Tokyo, 7-3-1 Hongo, Bunkyo-ku, Tokyo 113-0033, Japan.

Corresponding authors' e-mail addresses: simon.chorazy@uj.edu.pl; barbara.sieklucka@uj.edu.pl

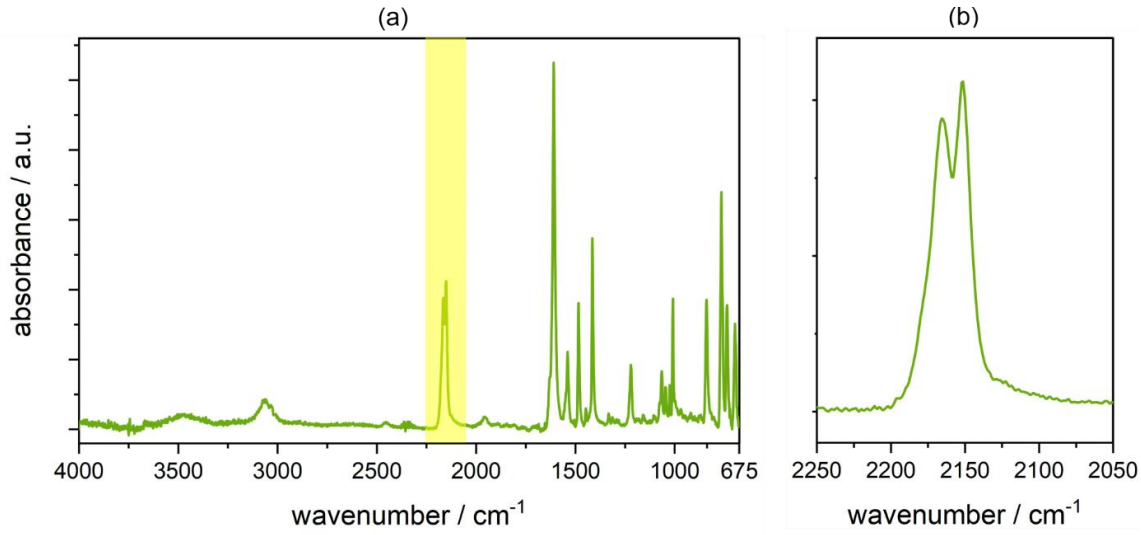

Fig. S1 Infrared (IR) absorption spectra of **1**^{air}, presented in the 4000–675 cm^{-1} range (a), and the enlargement of the 2250–2050 cm^{-1} region related to the stretching vibrations of cyanido ligands (b).[S1–S2]

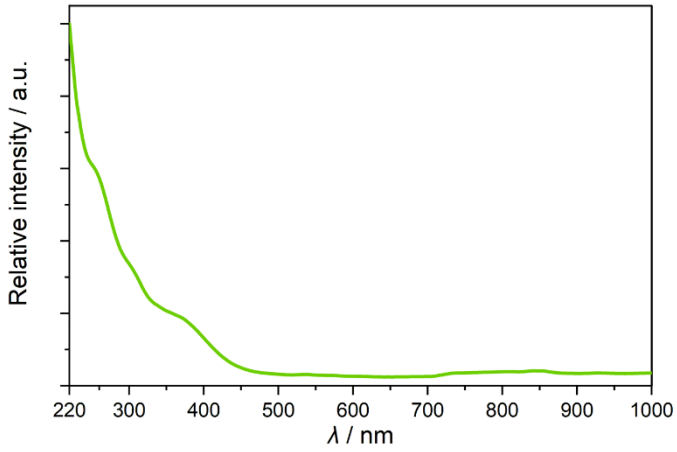

Fig. S2 Room-temperature solid-state UV-vis-NIR absorption spectra for **1**^{air} measured in the 200–1000 nm wavelength range.

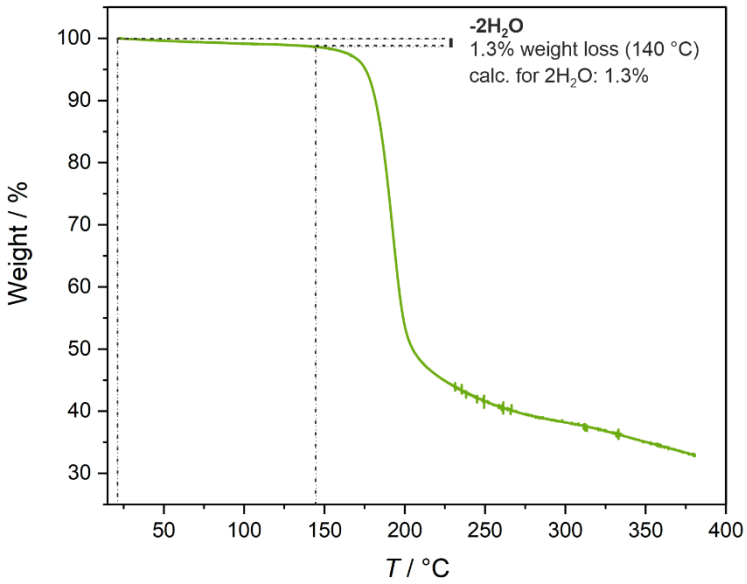

Fig. S3 Thermogravimetric (TG) curve of **1**^{air} measured under a nitrogen atmosphere upon the continuous heating with the 1 °C·min^{-1} rate. The step related to the heating-induced removal of solvent molecules (i.e., two water molecules of crystallization per the formula unit) is indicated on the graph.

Table S1 Details of crystal data and structure refinement of **1^{sol}** at various indicated temperatures.

crystalline phase	**1^{sol}**		
T / K	90	140	220
formula	$Fe_3Re_2C_{149}N_{28}O_2H_{108}$		
formula weight / g·mol^{-1}	2862.58	2862.58	2862.58
λ / Å	0.71075	0.71075	0.71075
crystal system	monoclinic	monoclinic	monoclinic
space group	$P2_1/c$	$P2_1/c$	$P2_1/c$
a / Å	15.4472(5)	15.4680(3)	15.4875(3)
b / Å	28.7353(10)	28.4622(6)	28.5837(5)
c / Å	15.4503(5)	15.8613(4)	15.9498(3)
β / deg	108.913(8)	108.668(8)	108.302(8)
V / Å^3	6487.8(5)	6615.6(4)	6703.6(4)
Z	2	2	2
calculated density / g·cm^{-3}	1.465	1.437	1.418
absorption coefficient	2.252	2.209	2.18
F(000)	2884	2884	2884
crystal shape	block	block	block
crystal's color	red	orange	green
crystal size / mm×mm×mm	0.31×0.27×0.21	0.31×0.27×0.21	0.31×0.27×0.21
Θ range / deg	3.034-25.351	3.034-25.35	3.029-25.35
limiting indices	-18 < h < 18 -34 < k < 32 -18 < l < 18	-18 < h < 18 -34 < k < 30 -19 < l < 19	-18 < h < 18 -34 < k < 31 -19 < l < 19
collected reflections	49853	50574	52886
unique reflections	11855	12078	12248
R_{int}	0.0915	0.0608	0.0481
completeness	0.997	0.998	0.998
data/restraints/ parameters	11855/43/844	12078/13/844	12248/7/844
GOF on F^2	1.166	1.173	1.227
final R indices	R_1 = 0.0731 [I > 2σ(I)] wR_2 = 0.1561 (all data)	R_1 = 0.0550 [I > 2σ(I)] wR_2 = 0.1074 (all data)	R_1 = 0.0490 [I > 2σ(I)] wR_2 = 0.0902 (all data)
largest diffraction peak and hole / e·Å^{-3}	1.925 and –1.815	1.184 and –1.586	0.701 and –1.624

Table S2 Detailed structure parameters for the coordination skeletons of **1**^{sol} at various indicated temperatures.

parameter (bond or angle)	**1**^{sol}		
	90 K	140 K	220
Fe1–N1 / Å	1.966(8)	2.122(5)	2.147(4)
Fe1–N3 / Å	1.966(8)	2.109(5)	2.142(4)
Fe1–N9 / Å	2.062(8)	2.213(5)	2.243(4)
Fe1–N10 / Å	2.033(7)	2.184(5)	2.219(4)
Fe1–N11 / Å	2.050(7)	2.185(5)	2.220(4)
Fe1–N12 / Å	2.014(8)	2.149(6)	2.179(5)
Fe2–N2 / Å	2.173(8)	2.163(5)	2.164(4)
Fe2–N13 / Å	2.248(8)	2.256(5)	2.253(5)
Fe2–N14 / Å	2.189(7)	2.190(6)	2.198(5)
Re1–C1 / Å	2.100(9)	2.080(6)	2.092(5)
Re1–C2 / Å	2.088(9)	2.098(6)	2.096(5)
Re1–C3 / Å	2.112(10)	2.089(6)	2.083(5)
Re1–C4 / Å	2.111(9)	2.113(6)	2.117(5)
Re1–C5 / Å	2.109(10)	2.112(6)	2.114(5)
Re1–C6 / Å	2.086(10)	2.110(6)	2.116(5)
Re1–C7 / Å	2.102(10)	2.113(7)	2.105(6)
Re1–C8 / Å	2.106(10)	2.111(7)	2.116(6)
Fe1–Re1 / Å	5.194 5.209	5.346 5.339	5.374 5.365
Fe2–Re1 / Å	5.389	5.373	5.378
Fe1–Fe1 / Å	7.725	7.932	7.979
Fe1–Fe2 / Å	8.260 9.960	8.298 10.058	8.344 10.085
N1-Fe1-N3/deg	177.4(3)	178.04	178.33(16)
N2-Fe2-N2/deg	180.0(3)	180.00	180.0(2)
C1-Re1-C2 /deg	99.2(3)	97.5(2)	97.31(19)
C1-Re1-C3 /deg	91.8(3)	92.7(2)	93.05(18)
C2-Re1-C3 /deg	145.8(3)	145.8(2)	145.80(18)
Fe1-Re1-Fe1 /deg	95.91	95.87	95.96
Fe1-Re1-Fe2 /deg	102.59 140.04	101.46 139.75	101.81 139.70
Re1-Fe1-Re1 /deg	173.67	173.37	173.03
Re1-Fe2-Re1 /deg	180.00	180.00	180.00

Table S3 Details of crystal data and structure refinement of **1^{air}** at various indicated temperatures.

crystalline phase	**1^{air}**					
T / K	85	140	182 (heating)	182 (cooling)	220	298
formula	$Fe_3Re_2C_{148}N_{28}O_2H_{108}$					
formula weight / g·mol^{-1}	2850.57	2850.57	2850.57	2850.57	2850.57	2850.57
λ / Å	0.71073	0.71073	0.71073	0.71073	0.71073	0.71073
crystal system	monoclinic	monoclinic	monoclinic	monoclinic	monoclinic	monoclinic
space group	$P2_1/c$	$P2_1/c$	$P2_1/c$	$P2_1/c$	$P2_1/c$	$P2_1/c$
a / Å	15.4144(7)	15.4029(6)	15.4168(7)	15.2871(6)	15.3294(9)	15.4053(17)
b / Å	28.7109(13)	28.7762(12)	28.8377(14)	28.5177(12)	28.5919(17)	28.724(3)
c / Å	15.3458(7)	15.3905(6)	15.4400(8)	15.8503(6)	15.8731(10)	15.9122(17)
β / deg	108.8800(10)	107.3250(10)	107.4650(10)	107.2210(10)	107.312(2)	107.602(3)
V / Å^3	6426.1(5)	6512.1(5)	6547.9(6)	6600.2(5)	6642.0(7)	6711.5(13)
Z	2	2	2	2	2	2
calculated density / g·cm^{-3}	1.473	1.454	1.446	1.434	1.425	1.411
absorption coefficient	2.274	2.244	2.231	2.214	2.2	2.177
F(000)	2872	2872	2872	2872	2872	2872
crystal shape	block	block	block	block	block	block
crystal's color	red	red	red	green	green	green
crystal size / mm×mm×mm	0.54×0.34 ×0.10	0.54×0.34 ×0.10	0.54×0.34 ×0.10	0.54×0.34 ×0.10	0.54×0.34 ×0.10	0.54×0.34 ×0.10
Θ range / deg	2.545-25.166	2.535-26.731	2.53-26.731	2.53-26.732	2.525-26.733	2.516-26.733
limiting indices	-18 < h < 18 -34 < k < 34 -18 < l < 18	-19 < h < 19 -36 < k < 36 -19 < l < 19	-19 < h < 19 -36 < k < 36 -19 < l < 19	-19 < h < 19 -35 < k < 36 -20 < l < 19	-19 < h < 19 -36 < k < 36 -20 < l < 19	-19 < h < 19 -36 < k < 36 -19 < l < 20
collected reflections	64278	73234	75069	78297	78448	79540
unique reflections	11503	13798	13883	13957	14055	14226
R_{int}	0.0328	0.0298	0.0277	0.0222	0.023	0.0254
completeness	0.997	0.997	0.997	0.997	0.997	0.997
data/restraints/ parameters	11503/30/ 835	13798/131/ 949	13883/139/ 847	13957/77/ 931	14055/69/ 931	14226/45/ 931
GOF on F^2	1.056	1.088	1.064	1.092	1.088	1.083
final R indices	R_1 = 0.0402 [I > 2σ(I)] wR_2 = 0.1031 (all data)	R_1 = 0.0486 [I > 2σ(I)] wR_2 = 0.1325 (all data)	R_1 = 0.0573 [I > 2σ(I)] wR_2 = 0.1694 (all data)	R_1 = 0.0320 [I > 2σ(I)] wR_2 = 0.0795 (all data)	R_1 = 0.0281 [I > 2σ(I)] wR_2 = 0.0720 (all data)	R_1 = 0.0247 [I > 2σ(I)] wR_2 = 0.0602 (all data)
largest diffraction peak and hole / e·Å^{-3}	1.969 and –1.053	2.074 and –1.250	2.844 and –1.352	1.335 and –1.206	1.049 and –0.986	0.687 and –0.719

Table S4 Detailed structure parameters for the coordination skeletons of **1**^{air} at various indicated temperatures.

parameter (bond or angle)	**1**^{air}					
	85 K	140 K	182 K (heating)	182 K (cooling)	220 K	298 K
Fe1–N1 / Å	1.930(4)	2.024(5)	2.035(6)	2.129(3)	2.136(3)	2.141(2)
Fe1–N3 / Å	1.934(4)	2.025(5)	2.039(6)	2.127(3)	2.134(3)	2.139(2)
Fe1–N9 / Å	2.026(5)	2.113(6)	2.121(8)	2.242(4)	2.247(3)	2.251(3)
Fe1–N10 / Å	2.011(4)	2.110(5)	2.126(5)	2.230(4)	2.237(3)	2.238(3)
Fe1–N11 / Å	2.017(4)	2.112(5)	2.127(6)	2.205(3)	2.212(3)	2.222(2)
Fe1–N12 / Å	1.999(4)	2.084(7)	2.109(9)	2.192(4)	2.196(3)	2.202(3)
Fe2–N2 / Å	2.171(4)	2.165(5)	2.168(5)	2.155(3)	2.158(3)	2.168(2)
Fe2–N13 / Å	2.256(4)	2.250(5)	2.255(6)	2.244(4)	2.248(3)	2.250(3)
Fe2–N14 / Å	2.195(4)	2.208(5)	2.209(5)	2.204(4)	2.205(3)	2.208(3)
Re1–C1 / Å	2.091(5)	2.088(5)	2.086(6)	2.085(3)	2.083(3)	2.087(3)
Re1–C2 / Å	2.101(5)	2.103(6)	2.106(6)	2.096(3)	2.098(3)	2.098(3)
Re1–C3 / Å	2.099(5)	2.090(6)	2.090(6)	2.087(3)	2.089(3)	2.089(2)
Re1–C4 / Å	2.119(5)	2.122(5)	2.127(6)	2.120(3)	2.121(3)	2.121(3)
Re1–C5 / Å	2.112(5)	2.115(6)	2.111(7)	2.109(4)	2.109(3)	2.111(3)
Re1–C6 / Å	2.122(5)	2.118(5)	2.117(6)	2.114(4)	2.118(3)	2.116(3)
Re1–C7 / Å	2.106(5)	2.107(6)	2.100(7)	2.101(4)	2.102(4)	2.098(3)
Re1–C8 / Å	2.118(5)	2.117(6)	2.110(7)	2.116(3)	2.118(3)	2.121(3)
Fe1–Re1 / Å	5.162 5.171	5.246 5.247	5.261 5.260	5.350 5.335	5.357 5.344	5.365 5.354
Fe2–Re1 / Å	5.380	5.371	5.370	5.353	5.358	5.367
Fe1–Fe1 / Å	7.674	7.699	7.724	7.933	7.945	7.964
Fe1–Fe2 / Å	8.225 9.916	8.288 9.982	8.308 9.988	8.303 10.041	8.323 10.051	8.344 10.065
N1-Fe1-N3/deg	177.42(17)	178.87(19)	178.7(2)	178.92(15)	178.82(13)	178.56(10)
N2-Fe2-N2/deg	180.00	180.00(17)	180.00(19)	180.00(16)	180.00	180.00
C1-Re1-C2 /deg	98.15(18)	97.8(2)	97.4(2)	95.59(14)	95.83(12)	95.91(10)
C1-Re1-C3 /deg	91.70(18)	91.0(2)	91.4(2)	94.24(13)	94.13(12)	94.16(10)
C2-Re1-C3 /deg	145.51(17)	145.74(19)	145.6(2)	145.79(13)	145.78(11)	145.68(10)
Fe1-Re1-Fe1 /deg	95.91	94.39	94.46	95.88	95.87	95.96
Fe1-Re1-Fe2 /deg	102.55 140.06	102.62 140.13	102.79 139.95	101.74 139.88	101.94 139.84	102.06 139.71
Re1-Fe1-Re1 /deg	173.83	174.09	174.11	172.79	172.77	173.13
Re1-Fe2-Re1 /deg	180.00	180.00	180.00	180.00	180.00	180.00

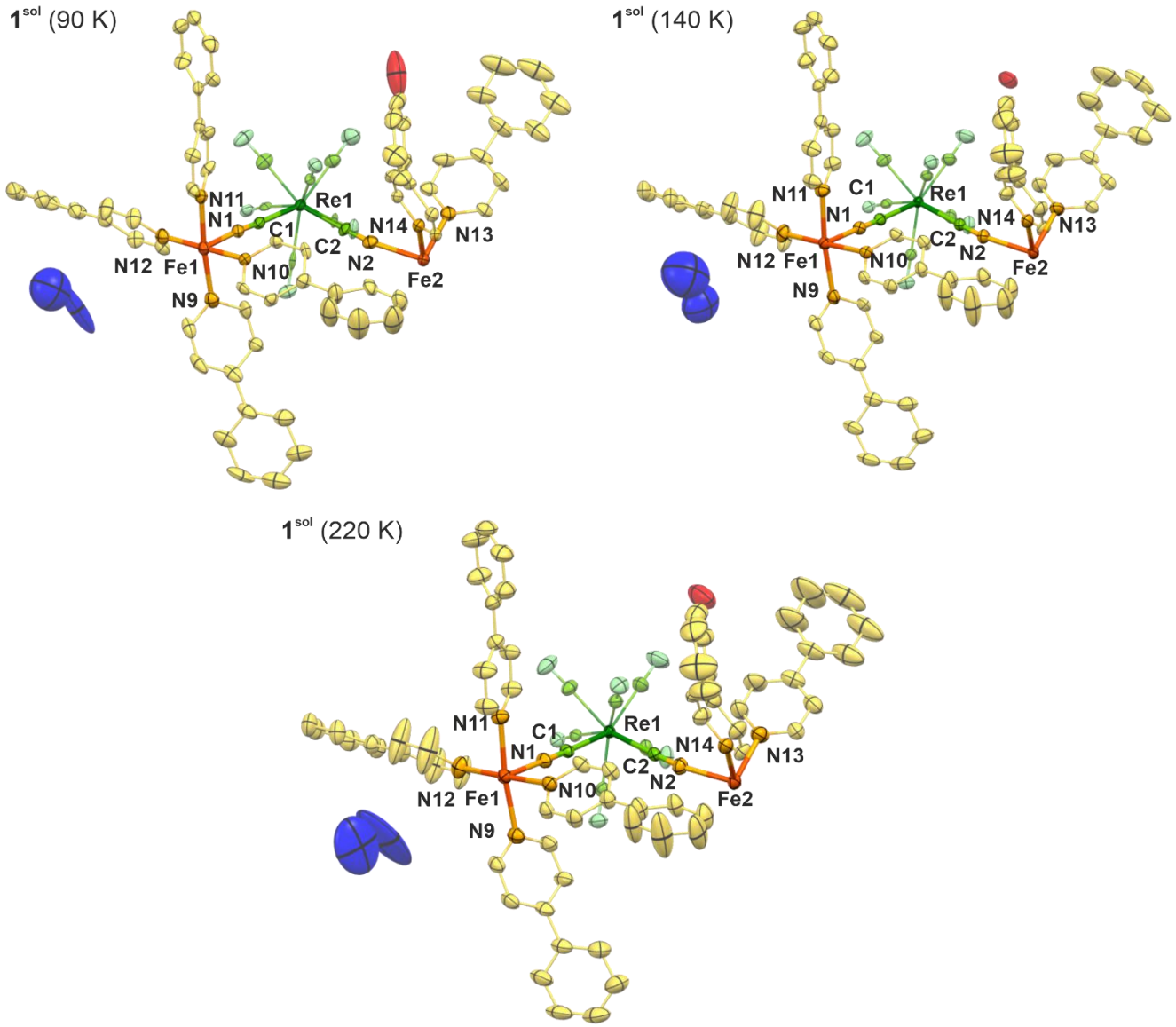

Fig. S4 Views of the asymmetric units of **1**^{sol} at various indicated temperatures. Thermal ellipsoids are presented at the 50% probability level. Hydrogen atoms were omitted for clarity. Colors: Fe centers with the coordinated nitrogen atoms – dark and lighter orange, respectively; Re centers with the coordinated carbon atoms – dark and lighter green, respectively; nitrogen atoms of terminal cyanido ligands – very light green; carbon atoms of 4-phpy ligands – yellow; water molecules of crystallization – red; methanol molecules of crystallization – blue. The labeling scheme was provided for metal centers, atoms directly attached to Fe centers, and atoms of bridging cyanido ligands.

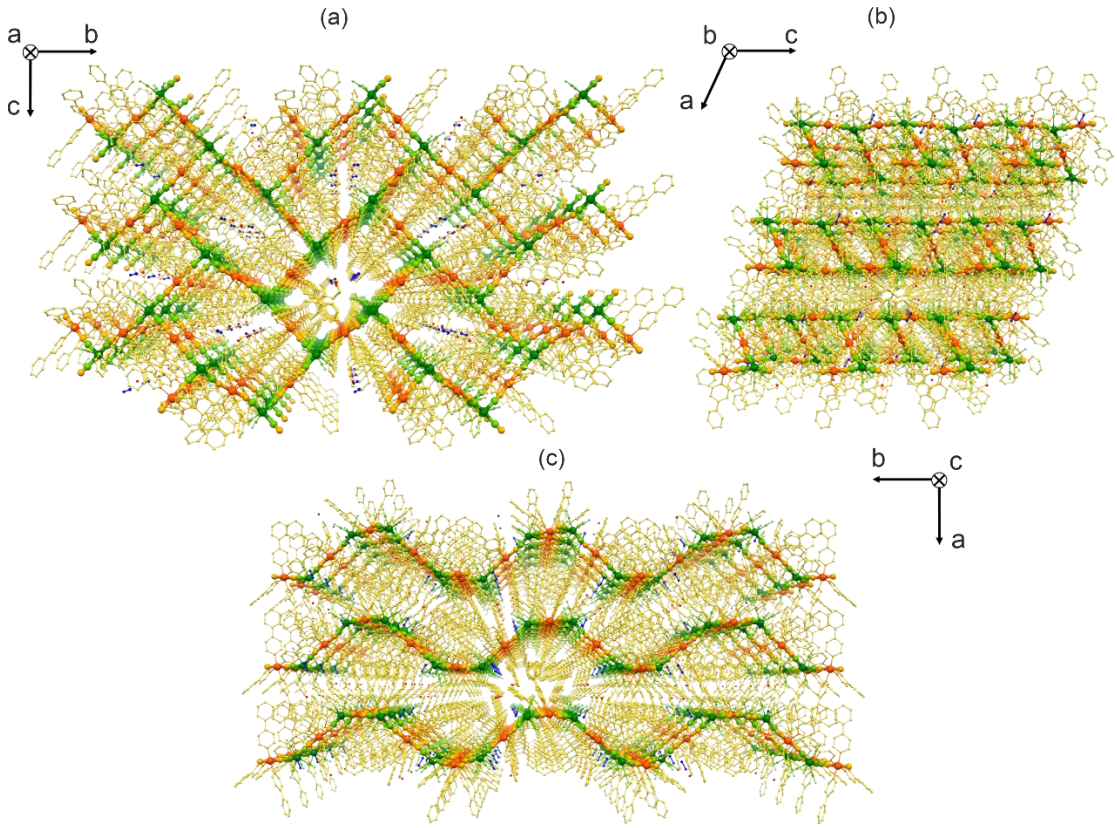

Fig. S5 Supramolecular arrangement of coordination layers of **1**^{sol} (for data gathered at 90 K) presented within *bc* (a), *ac* (a), and *ab* (c) crystallographic planes. Colors: Fe centers with the coordinated nitrogen atoms – dark and lighter orange, respectively; Re centers with the coordinated carbon atoms – dark and lighter green, respectively; nitrogen atoms of terminal cyanido ligands – very light green; carbon atoms of 4-phpy ligands – yellow; water molecules of crystallization – red; methanol molecules of crystallization – blue.

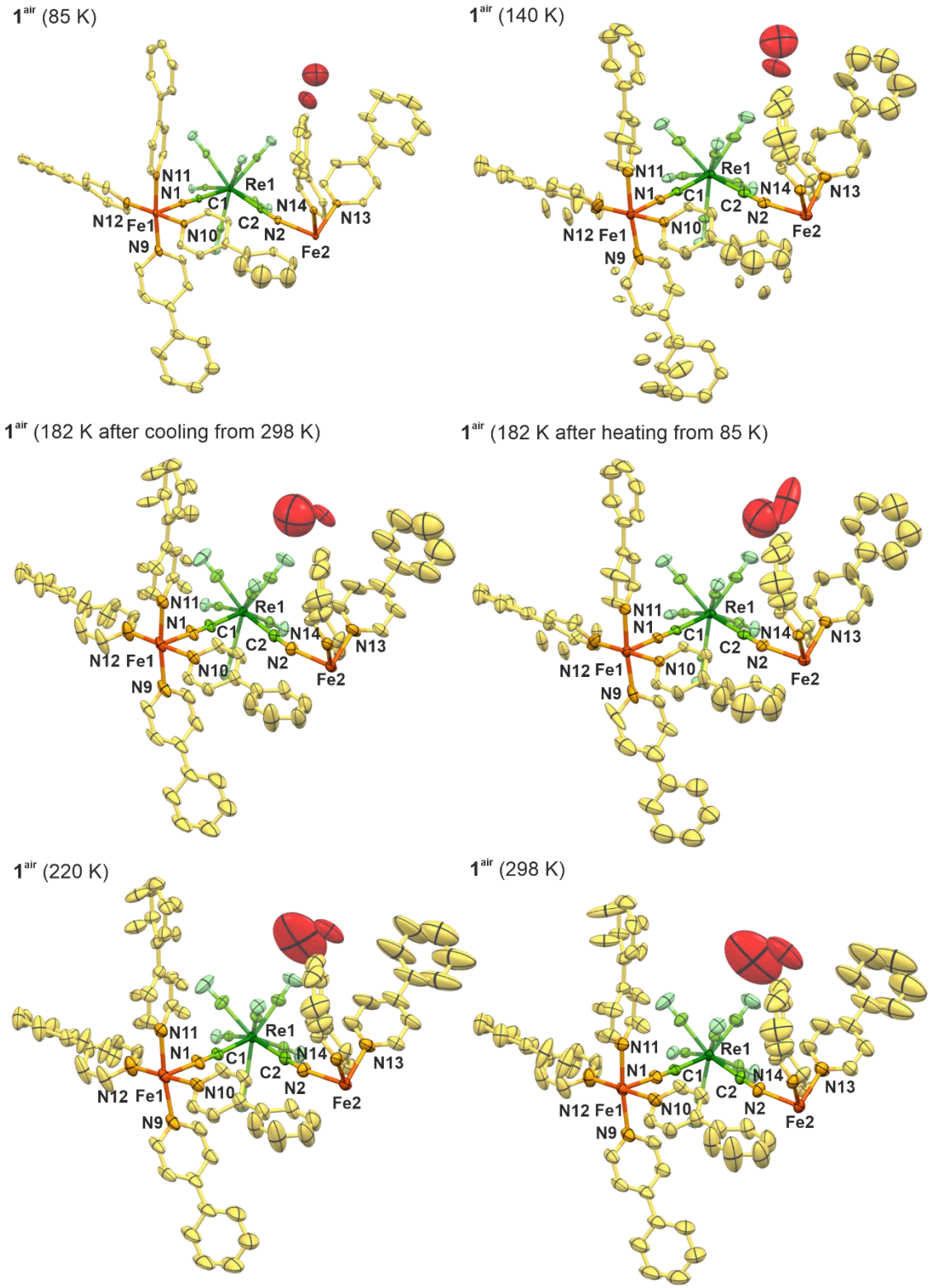

Fig. S6 Views of the asymmetric units of **1**^{air} at various indicated temperatures. Thermal ellipsoids are presented at the 50% probability level. Hydrogen atoms were omitted for clarity. Colors: Fe centers with the coordinated nitrogen atoms – dark and lighter orange, respectively; Re centers with the coordinated carbon atoms – dark and lighter green, respectively; nitrogen atoms of terminal cyanido ligands – very light green; carbon atoms of 4-phpy ligands – yellow; water molecules of crystallization – red. The labeling scheme was provided for metal centers, atoms directly attached to Fe centers, and atoms of bridging cyanido ligands.

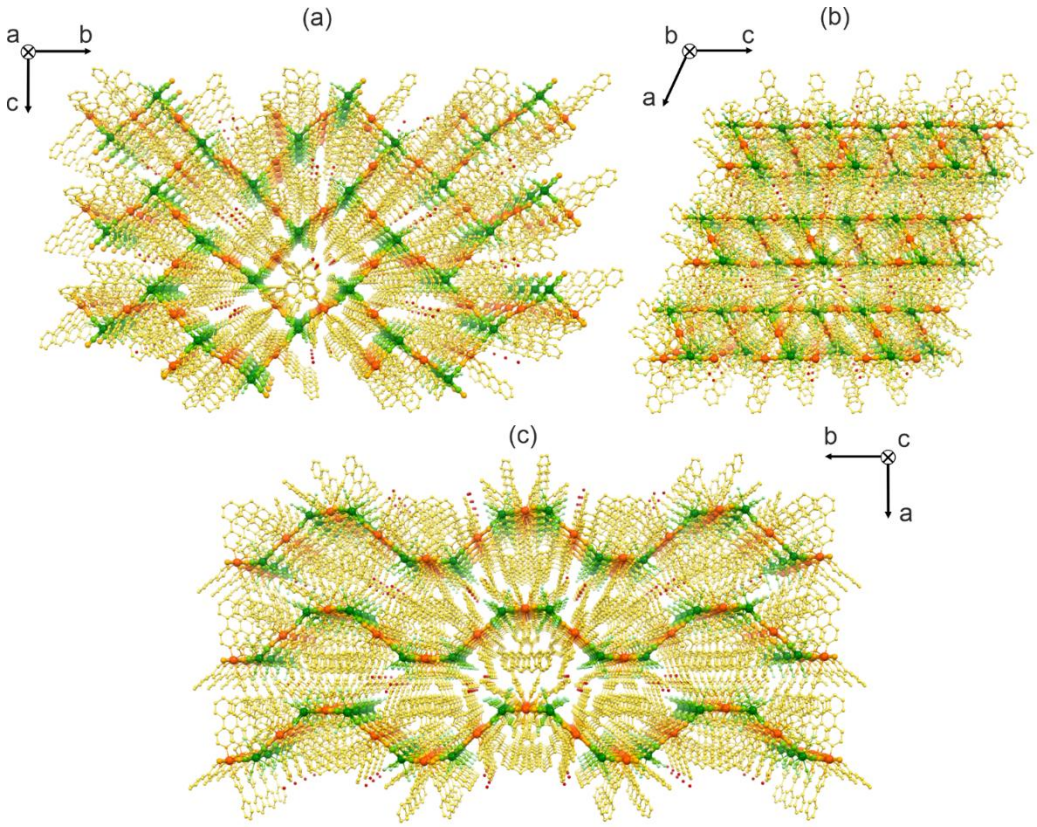

Fig. S7 Supramolecular arrangement of coordination layers of **1**^{airl} (for data gathered at 85 K) presented within *bc* (a), *ac* (a), and *ab* (c) crystallographic planes. Colors: Fe centers with the coordinated nitrogen atoms – dark and lighter orange, respectively; Re centers with the coordinated carbon atoms – dark and lighter green, respectively; nitrogen atoms of terminal cyanido ligands – very light green; carbon atoms of 4-phpy ligands – yellow; water molecules of crystallization – red.

Table S5 Results of Continuous Shape Measure Analysis (CShM) for six-coordinated $[Fe^{II}(4\text{-phpy})_4(NC)_2]$ complexes in **1**^{sol} at various indicated temperatures.[S3–S5] Note that S = 0 corresponds to the ideal polyhedron, and this parameter increases upon the increasing deformation from the ideal given geometry.

1^{sol}	S_{PPY} (pentagonal pyramid)	S_{OC} (octahedron)	S_{TPR} (trigonal prism)
$[Fe1(4\text{-phpy})_4(NC)_2]$ (90 K)	27.975	0.162	14.652
$[Fe2(4\text{-phpy})_4(NC)_2]$ (90 K)	30.048	0.025	16.616
$[Fe1(4\text{-phpy})_4(NC)_2]$ (140 K)	27.821	0.175	14.481
$[Fe2(4\text{-phpy})_4(NC)_2]$ (140 K)	29.727	0.055	16.487
$[Fe1(4\text{-phpy})_4(NC)_2]$ (220 K)	27.906	0.171	14.538
$[Fe2(4\text{-phpy})_4(NC)_2]$ (220 K)	29.677	0.055	16.491

Table S6 Results of Continuous Shape Measure Analysis (CShM) for eight-coordinated $[Re^{V}(CN)_8]^{3-}$ complexes in **1**^{sol} at various indicated temperatures.[S3–S5] Note that S = 0 corresponds to the ideal polyhedron, and this parameter increases upon the increasing deformation from the ideal given geometry.

1^{sol}	S_{SAPR} (square antiprism)	S_{TDD} (triangular dodecahedron)	S_{BTPR} (bicapped trigonal prism)
$[Re1(CN)_8]^{3-}$ (90 K)	1.899	0.272	2.089
$[Re1(CN)_8]^{3-}$ (140K)	2.082	0.265	2.071
$[Re1(CN)_8]^{3-}$ (220 K)	2.239	0.233	2.230

Table S7 Results of Continuous Shape Measure Analysis (CShM) for six-coordinated $[Fe^{II}(4\text{-phpy})_4(NC)_2]$ complexes in **1**^{air} at various indicated temperatures.[S3–S5] Note that S = 0 corresponds to the ideal polyhedron, and this parameter increases upon the increasing deformation from the ideal given geometry.

1^{air}	S_{PPY} (pentagonal pyramid)	S_{OC} (octahedron)	S_{TPR} (trigonal prism)
$[Fe1(4phpy)_4(NC)_2]$ (85 K)	28.256	0.145	14.985
$[Fe2(4phpy)_4(NC)_2]$ (85 K)	29.940	0.031	16.653
$[Fe1(4phpy)_4(NC)_2]$ (140K)	28.770	0.120	15.277
$[Fe2(4phpy)_4(NC)_2]$ (140 K)	29.966	0.028	16.617
$[Fe1(4phpy)_4(NC)_2]$ (182 K) (after heating from 85 K)	28.800	0.118	15.328
$[Fe2(4phpy)_4(NC)_2]$ (182 K) (after heating from 85 K)	29.973	0.029	16.642
$[Fe1(4phpy)_4(NC)_2]$ (182 K) (after cooling from 298 K)	28.335	0.167	14.890
$[Fe2(4phpy)_4(NC)_2]$ (182 K) (after cooling from 298 K)	29.709	0.047	16.510
$[Fe1(4phpy)_4(NC)_2]$ (220 K)	28.324	0.167	14.868
$[Fe2(4phpy)_4(NC)_2]$ (220 K)	29.712	0.049	16.535
$[Fe1(4phpy)_4(NC)_2]$ (298 K)	28.447	0.157	14.973
$[Fe2(4phpy)_4(NC)_2]$ (298 K)	29.781	0.038	16.550

Table S8 Results of Continuous Shape Measure Analysis (CShM) for eight-coordinated $[Re^{V}(CN)_8]^{3-}$ complexes in **1**^{air} at various indicated temperatures.[S3–S5] Note that S = 0 corresponds to the ideal polyhedron, and this parameter increases upon the increasing deformation from the ideal given geometry.

1^{air}	S_{SAPR} (square antiprism)	S_{TDD} (triangular dodecahedron)	S_{BTPR} (bicapped trigonal prism)
$[Re1(CN)_8]^{3-}$ (85 K)	1.959	0.257	2.02
$[Re1(CN)_8]^{3-}$ (140K)	1.944	0.294	1.978
$[Re1(CN)_8]^{3-}$ (182 K) (heating after 85 K)	2.030	0.270	2.041
$[Re1(CN)_8]^{3-}$ (182 K) (cooling after 298 K)	2.659	0.196	2.448
$[Re1(CN)_8]^{3-}$ (220 K)	2.595	0.200	2.409
$[Re1(CN)_8]^{3-}$ (298 K)	2.590	0.195	2.407

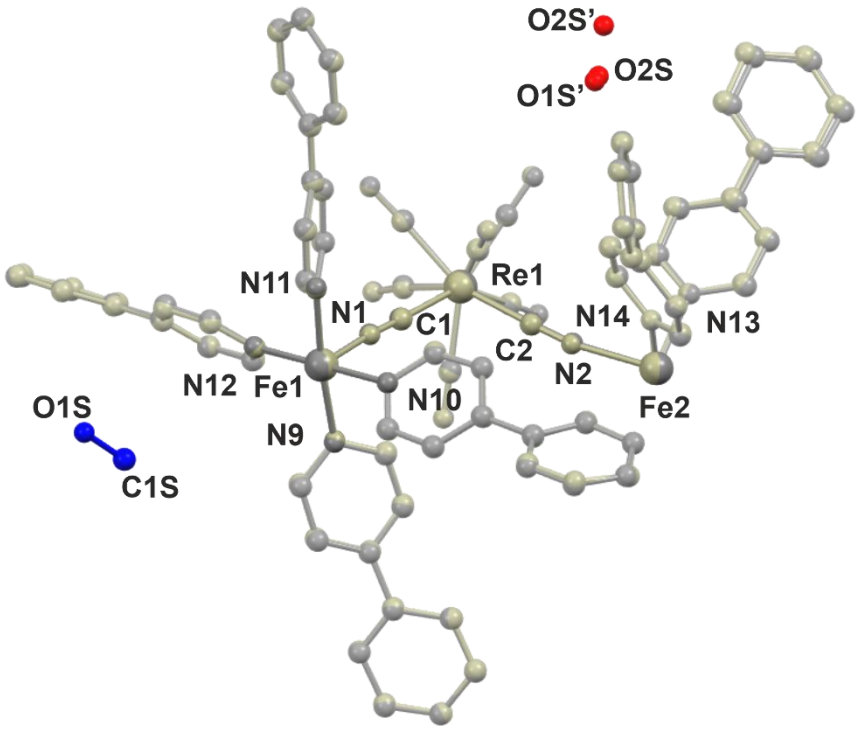

Fig. S8 Comparison of the asymmetric units of **1**^{sol} (*T* = 90 K) and **1**^{air} (*T* = 85 K) realized by overlapping of these two structures. Colors: coordination skeleton of **1**^{sol} – pale gray; coordination skeleton of **1**^{air} – dark gray; methanol molecules of **1**^{sol} – blue; water molecules of both structures – red (O2S corresponds to **1**^{sol} while O1S' and O2S' correspond to **1**^{air}).

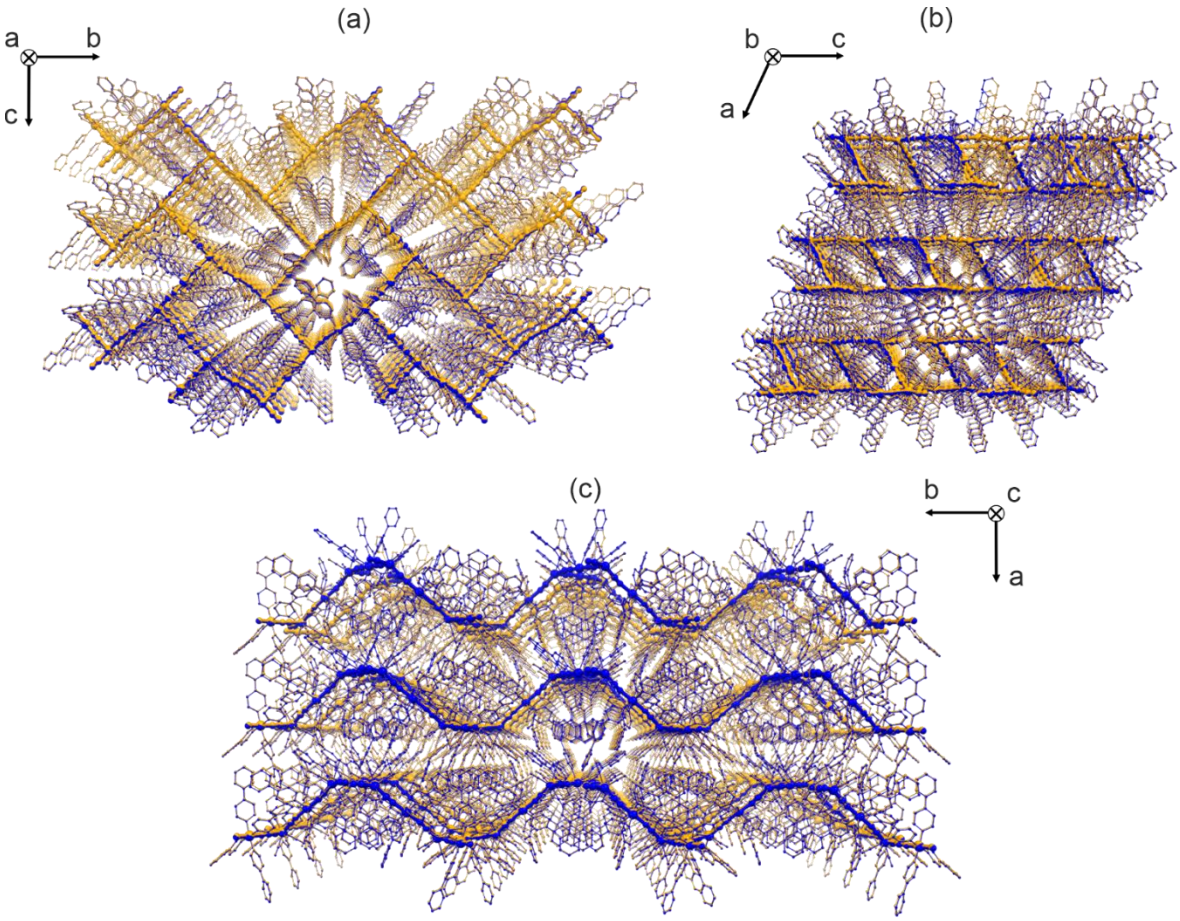

Fig. S9 Comparison of the coordination skeletons of $\mathbf{1}^{sol}$ (T = 90 K) and $\mathbf{1}^{air}$ (T = 85 K) realized by overlapping of these two structures that were visualized within the *bc* (a), *ac* (b), and *ab* (c) crystallographic planes. Colors: coordination skeleton of $\mathbf{1}^{sol}$ – blue; coordination skeleton of $\mathbf{1}^{air}$ – yellow.

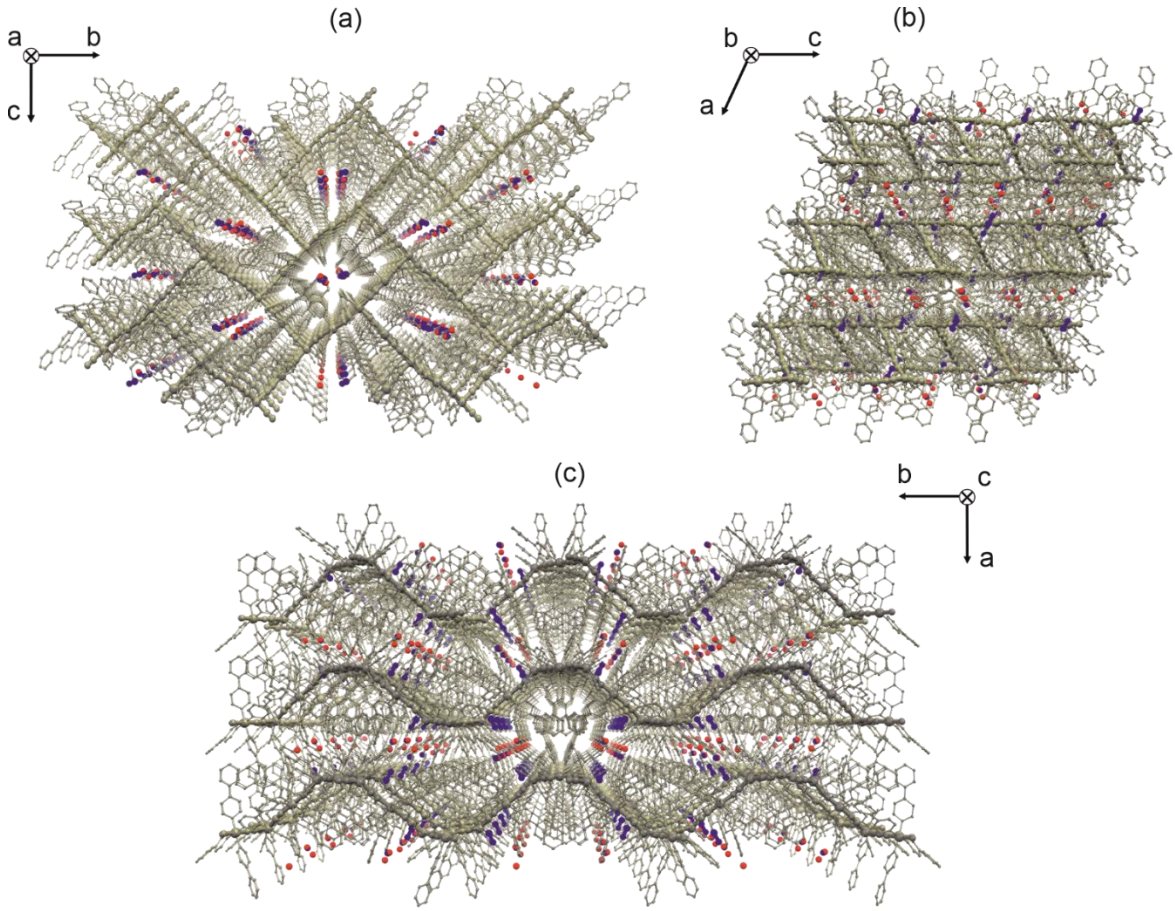

Fig. S10 Comparison of the arrangement of solvent molecules in **1**^{sol} (*T* = 90 K) and **1**^{air} (*T* = 85 K) realized by overlapping these two structures that were visualized within the *bc* (a), *ac* (b), and *ab* (c) crystallographic planes. Colors: coordination skeleton of **1**^{sol} – pale gray; coordination skeleton of **1air** – dark gray; methanol and water molecules of **1**^{sol} – blue; water molecules of **1**^{air} – red.

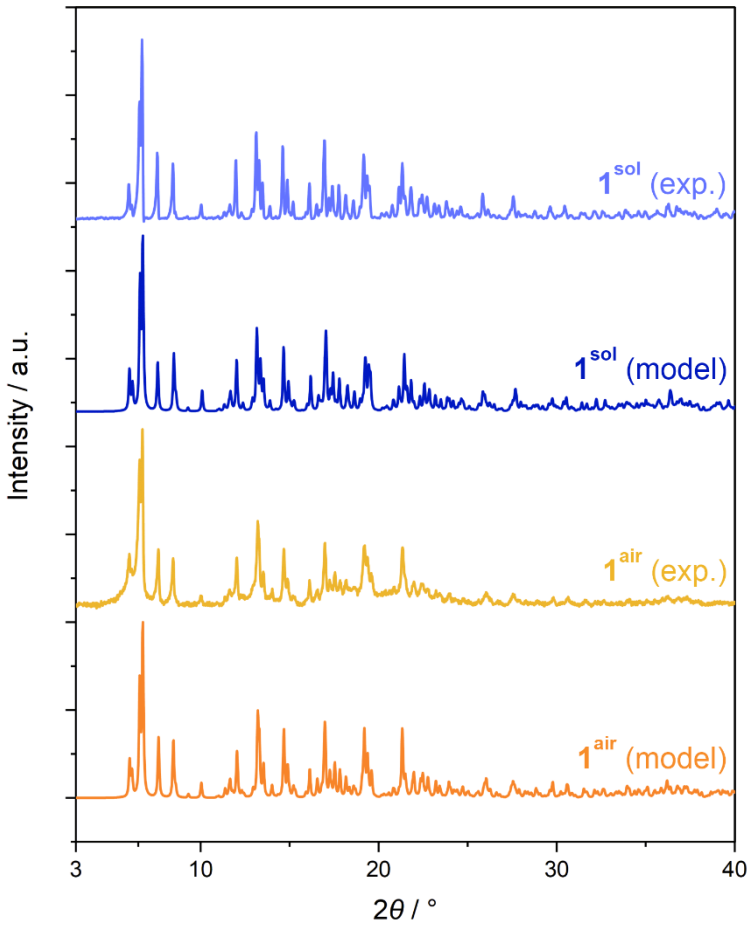

Fig. S11 Powder X-ray diffraction (P-XRD) patterns of **1**^{sol} and **1**^{air} measured at 300 K compared with the P-XRD patterns, calculated from respective structural models that were obtained from the single-crystal X-ray diffraction experiments (T = 220 K for **1**^{sol}, T = 298 K for **1**^{air}, see Tables S1 and S3).

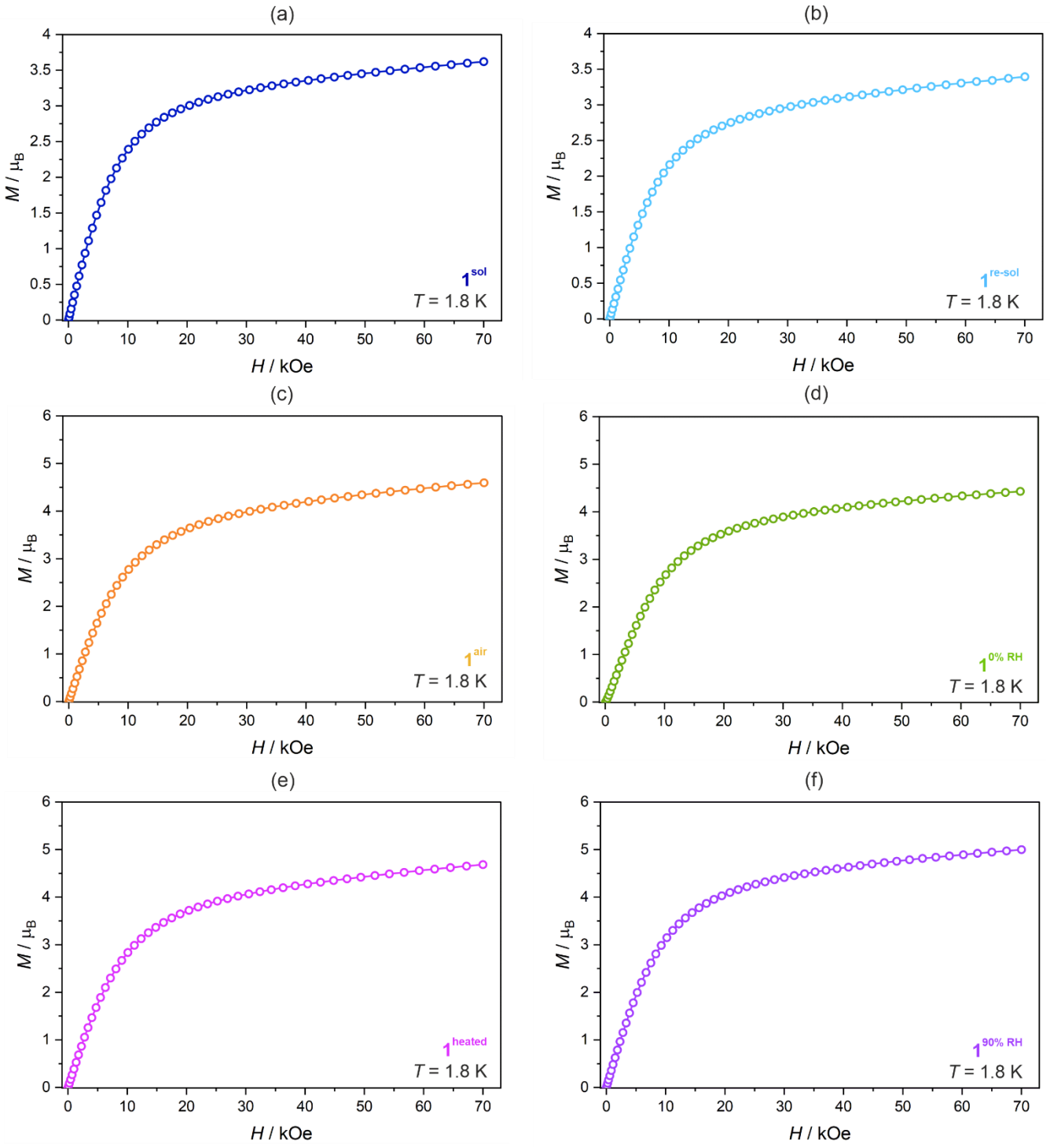

Fig. S12 Field-dependences of molar magnetization for various phases of **1**, including $\mathbf{1}^{sol}$ (a), $\mathbf{1}^{re\text{-}sol}$ (b), $\mathbf{1}^{air}$ (c), $\mathbf{1}^{0\%\ RH}$ (d), $\mathbf{1}^{heated}$ (e), and $\mathbf{1}^{90\%\ RH}$ (f).

Table S9 ^{57}Fe Mössbauer spectra parameters for **1**^{sol}.

T / K	Fe site	δ_{IS} / mm·s^{-1}	ΔE_Q / mm·s^{-1}	fraction / %	average Fe(II) spin (see Fig. 4)
180(1)↓ (cooling)	HS 1	1.10(1)	1.63(2)	36(2)	1.54(10)
	HS 2	1.09(1)	1.91(1)	41(2)	
	LS	0.42(1)	0.63(3)	23(2)	
140(1)↓	HS 1	1.15(1)	1.67(1)	34(3)	1.49(10)
	HS 2	1.11(1)	2.05(1)	40(3)	
	LS	0.42(2)	0.47(2)	26(2)	
110(1)↓	HS 1	1.20(1)	1.61(1)	34(2)	1.18(10)
	HS 2	1.12(1)	2.19(1)	25(2)	
	LS	0.41(1)	0.34(1)	41(2)	
85(1)	HS 1	1.21(1)	1.60(1)	29(2)	0.80(10)
	HS 2	1.14(1)	2.31(1)	11(2)	
	LS	0.45(1)	0.25(1)	60(2)	
110(1)↑ (heating)	HS 1	1.20(1)	1.59(1)	30(2)	1.06(10)
	HS 2	1.12(1)	2.20(1)	23(2)	
	LS	0.43(1)	0.30(1)	47(2)	
140(1)↑	HS 1	1.15(1)	1.66(1)	34(2)	1.51(10)
	HS 2	1.11(1)	2.04(1)	41(3)	
	LS	0.43(1)	0.46(2)	25(2)	
180(1)↑	HS 1	1.11(1)	1.63(1)	37(2)	1.57(10)
	HS2	1.10(1)	1.91(1)	42(2)	
	LS	0.41(1)	0.61(3)	21(2)	

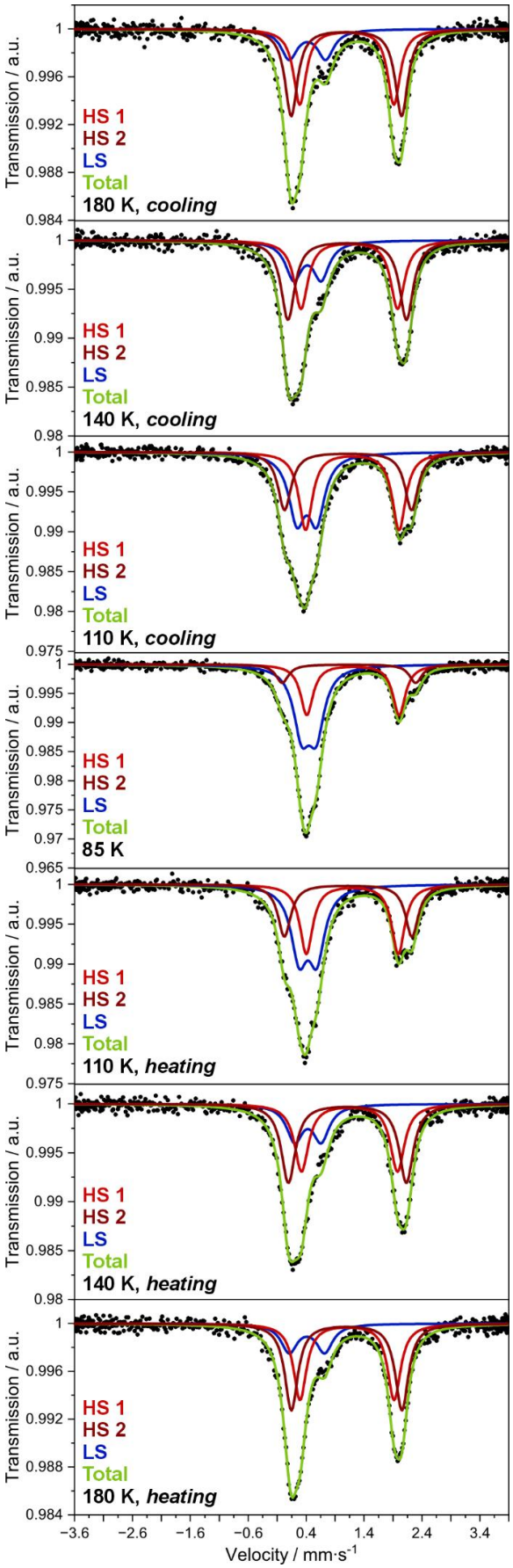

Fig. S13 Temperature-variable ^{57}Fe Mössbauer spectra of **1^{sol}** with the indicated contributions from three different Fe(II) sites (the high-spin states of HS1 and HS2, the low-spin state of LS). Experimental data is presented as black points while the best fits as solid lines with specific colors for HS and LS contributions and the total fit.

Fig. S10 ^{57}Fe Mössbauer spectra parameters for **1^{air}**.

T / K	Fe site	δ_{IS} / mm·s^{-1}	ΔE_Q / mm·s^{-1}	fraction / %	average Fe(II) spin (see Fig. 4)
220(1)↓ (cooling)	HS 1	1.07(2)	1.51(4)	30(4)	1.76(10)
	HS 2	1.09(1)	1.89(2)	58(6)	
	LS	0.27(6)	0.58(11)	12(4)	
180(1)↓	HS 1	1.09(1)	1.60(3)	40(4)	1.78(10)
	HS 2	1.10(1)	2.03(2)	49(5)	
	LS	0.34(7)	0.29(13)	11(3)	
140(1)↓	HS 1	1.25(2)	1.56(2)	35(4)	1.18(10)
	HS 2	1.13(1)	2.17(3)	24(3)	
	LS	0.33(3)	0.19(5)	41(2)	
85(1)	HS 1	1.29(2)	1.60(3)	32(3)	1.14(10)
	HS 2	1.14(1)	2.24(2)	25(3)	
	LS	0.37(2)	0.21(4)	43(2)	
140(1)↑ (heating)	HS 1	1.25(2)	1.57(3)	36(3)	1.18(10)
	HS 2	1.11(1)	2.21(2)	23(2)	
	LS	0.36(3)	0.23(5)	41(2)	
180(1)↑	HS 1	1.14(3)	1.53(3)	37(4)	1.68(10)
	HS 2	1.10(1)	2.00(3)	47(4)	
	LS	0.34(4)	0.21(10)	16(3)	
220(1)↑	HS 1	1.10(1)	1.48(5)	31(8)	1.76(10)
	HS 2	1.07(1)	1.90(3)	57(9)	
	LS	0.41(9)	0.38(19)	12(4)	

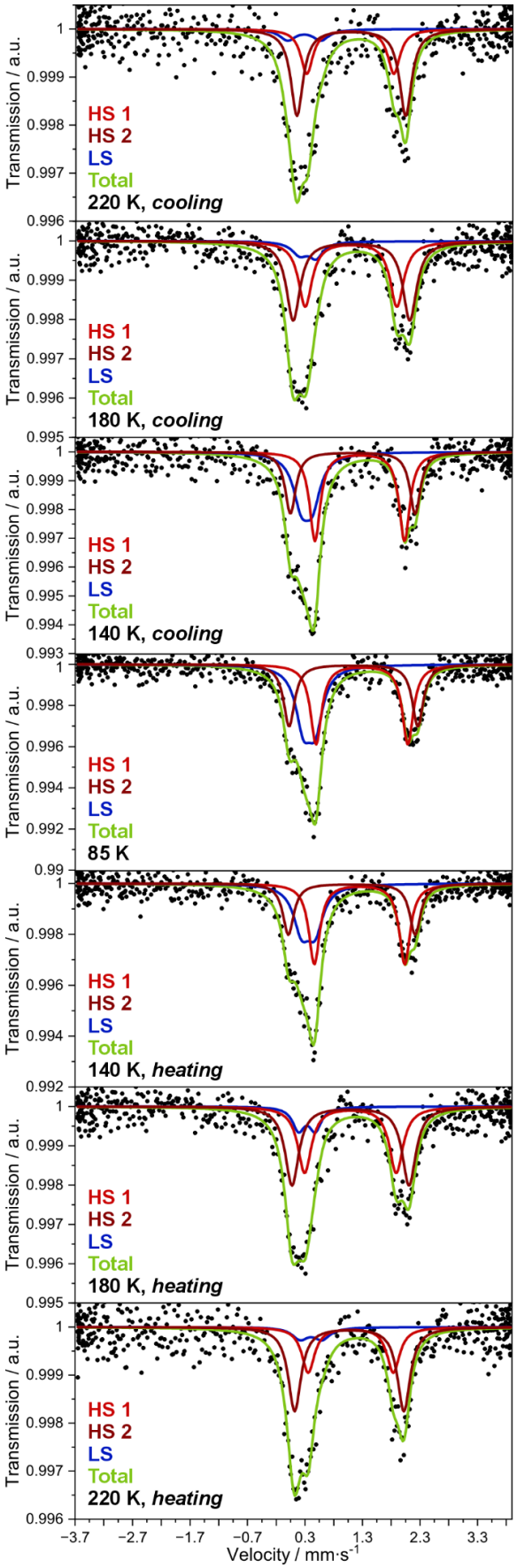

Fig. S14 Temperature-variable ^{57}Fe Mössbauer spectra of **1**^{air} with the indicated contributions from three different Fe(II) sites (the high-spin states of HS1 and HS2, the low-spin state of LS). Experimental data is presented as black points while the best fits as solid lines with specific colors for HS and LS contributions and the total fit.

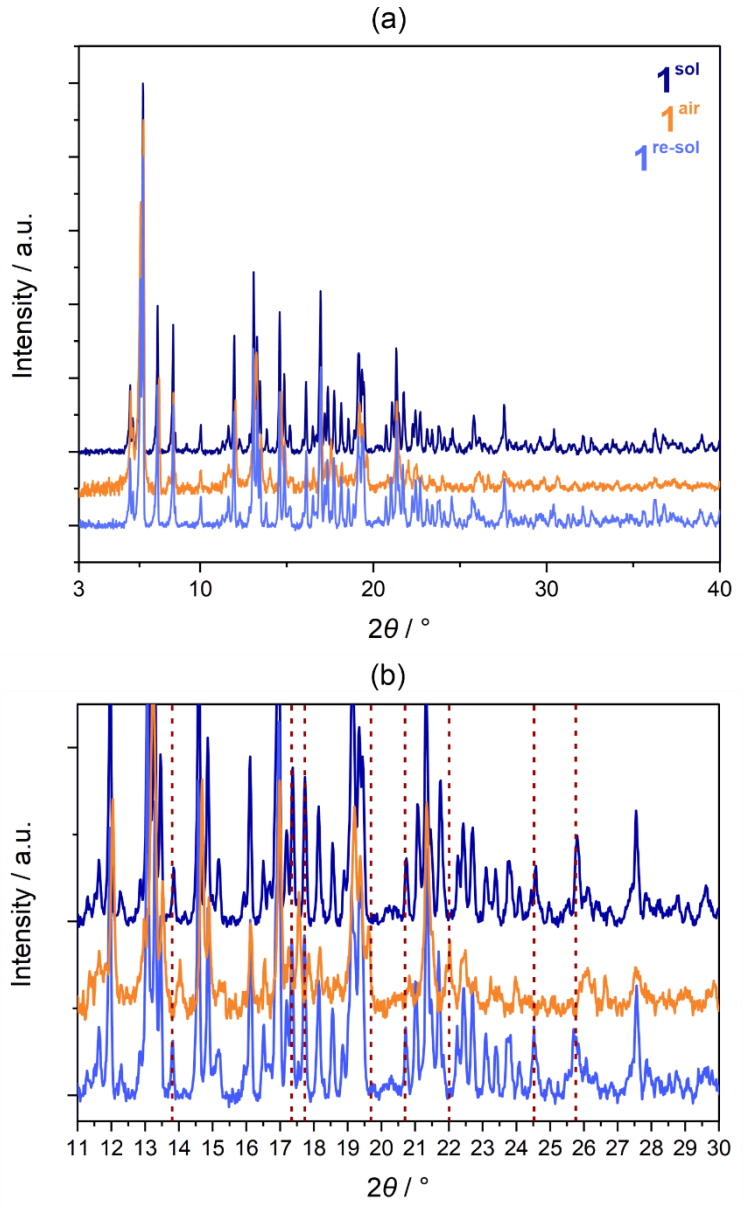

Fig. S15 Comparison of P-XRD patterns of **1**^{sol}, **1**^{air}, and **1**$^{re\text{-}sol}$, obtained by the subsequent treatment of the single batch of the powder sample of **1**, presented in the broader 3–40° range (a) and the enlarged view on the limited 11–30° range (b). The red dotted lines in (b) indicate the location of crucial differences between the phases.

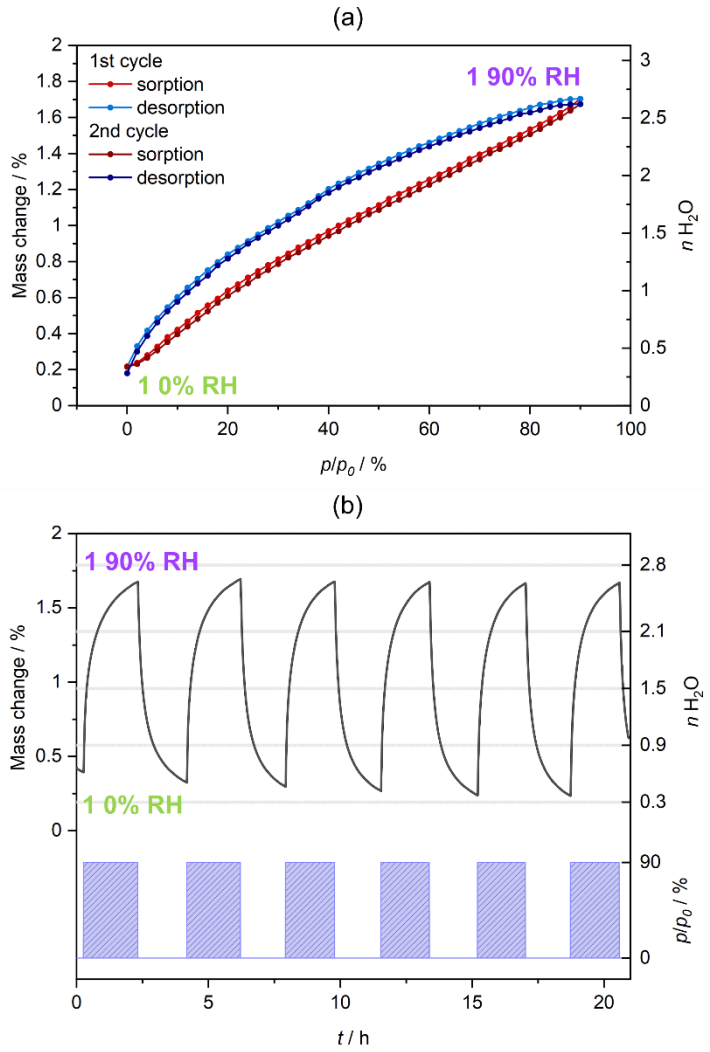

Fig. S16 Representative curves of water vapor sorption studies of **1**^{air}, including the isotherm of adsorption ranging between 0% and 90% relative humidity (RH) (a) and the curves depicting the switching between **1**$^{0\%\ RH}$ and **1**$^{90\%\ RH}$ phases for several 0–90% RH cycles (b).

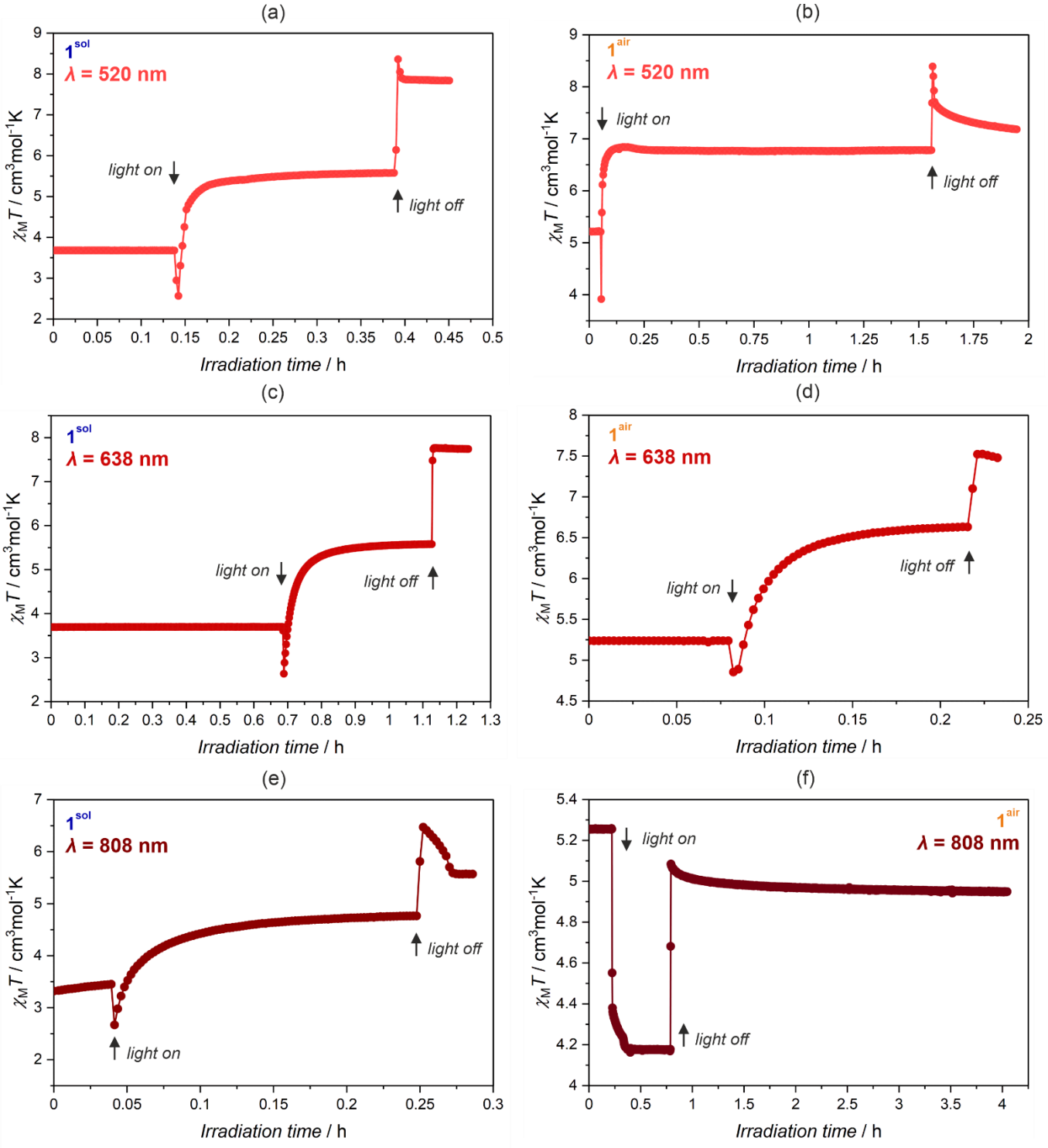

Fig. S17 Time dependences of the $\chi_M T$ product at 1000 Oe upon irradiation within the photomagnetic experiments (T = 10 K): using the 520 nm irradiation for **1**^{sol} (a), using the 520 nm irradiation for **1**^{air} (b), using the 638 nm irradiation for **1**^{sol} (c), using the 638 nm irradiation for **1**^{air} (d), using the 808 nm irradiation for **1**^{sol} (e), and using the 808 nm irradiation for **1**^{air} (f). The moments in time corresponding to turning on and off the light source have been indicated in the graphs.

Comment to Fig. S17:

In Fig. S17 time dependences of the $\chi_M T$ product at 10 K, visualizing the changes in magnetic signal upon the performed photomagnetic experiments, are presented. The related changes include the stable starting magnetic signal before the irradiation, its sudden change upon turning on the light (with the primary short-time drop due to the photo-induced heating effect), followed by its abrupt increase upon turning on the light which represents the thermal effect (recovery of the initial 10 K condition). Moreover, for all photomagnetic experiments, we kept the sample of **1**^{air} or **1**^{sol} after the photo-irradiation (i.e., after turning off the light) for at least several minutes to stabilize the signal that changes primarily due to the mentioned thermal effect. Moreover, this stabilization time was needed also to check the relaxation of the photo-induced state over time at 10 K (at which all the photo-irradiation experiments were performed). For each case (except the experiment related to the reverse-LIESST, Fig. S17f), we waited for several minutes which were found sufficient to detect the stable magnetic signal (thus, for sure, free of the thermal effects as the light was already off). Then, we started other magnetic studies by cooling to 2 K to perform the field-dependent magnetization measurements followed by collecting the temperature dependence (upon heating) of the magnetic moment (presented further in the form of the magnetic susceptibility–temperature product). For the case of **1**^{air}, for which the reverse-LIESST effect, manifested by the decrease of the magnetic signal after irradiation (which stayed in contrast to the results of all other photomagnetic experiments), was detected, we kept the sample at 10 K after irradiation for more than 3 hours. After turning off the 808 nm light, we observed primarily the sudden increase of the magnetic signal due to the thermal effect but its highest achieved level was still well below the starting value of the magnetic susceptibility–temperature product ($\chi_M T$). Then, we observed a subtle decrease in the magnetic signal (i.e., $\chi_M T$) which was followed by its stabilization over a longer time. Therefore, we could fully exclude the role of thermal effects on the observed magnetic signal, as the light was turned off and the sample was kept at 10 K for a very long time without any possible source of its heating. As a result, we are convinced that the observed overall decrease of the magnetic signal (observed primarily in the $\chi_M T$ value at 10 K, further in the magnetization versus magnetic field dependence, and finally in the $\chi_M T$ versus T plot upon heating the sample, Fig. 6, S18, and S19) after the 808 nm light irradiation is related to the reverse LIESST effect, not due to the irradiation-induced heating of the investigated sample.

Interestingly, for this special case of the reverse-LIESST effect induced by the 808 nm light irradiation for **1**^{air}, the shape of the $\chi_M T$ versus time plot after turning off the light was found to be very similar to the 520 nm light irradiation experiments and the 808 nm light irradiation for **1**^{sol}, thus for the cases of the typical LIESST effect. This similarity is related to the fast decrease in the $\chi_M T$ signal after the primary abrupt increase related to the temperature change upon turning off the light. For the cases of the typical LIESST effect, it could be ascribed to the partial relaxation of the photo-induced state of the material at 10 K. However, in the case of the reverse LIESST, such an effect should have resulted in a fast increase in the $\chi_M T$ signal as the relaxation should provide the higher $\chi_M T$ signal. This suggests that the photo-induced changes upon the 808 nm light irradiation are more complex as they can contain the LIESST effect for the part of the Fe(II) centers (e.g., those, for which the thermal SCO occurred) and the simultaneous reverse-LIESST for the other part of Fe(II) centers. In such a scenario, the $\chi_M T$ versus time plot can be of similar shape to the other irradiation wavelengths. Then, it can be postulated that the relaxation of a photo-induced state for the typical LIESST effect dominates and provides the observed decrease onto the $\chi_M T$ versus time plot after turning off and initial temperature stabilization while the reverse effect of the relaxation of the photo-induced state of the reverse LIESST is much weaker. Nevertheless, it is clearly observed that the main magnetic response of **1**^{air} to the 808 nm light irradiation is of a reverse LIESST character as the magnetic signal decreases upon this photo-irradiation in comparison to the pristine sample.

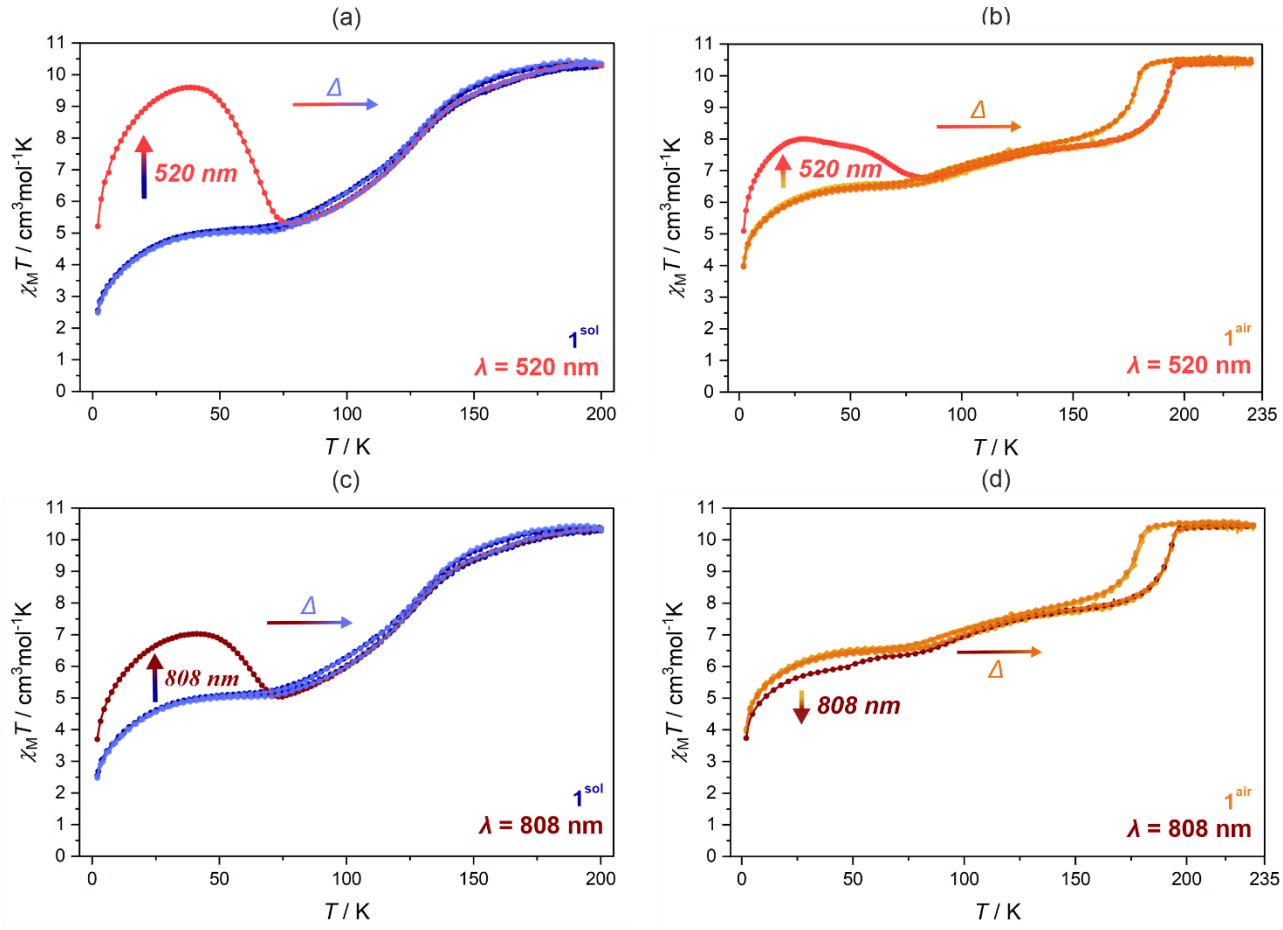

Fig. S18 Temperature dependences of the $\chi_M T$ product at 1000 Oe before and after irradiation: using the 520 nm light for **1**^{sol} (a), using the 520 nm light for **1**^{air} (b), using the 808 nm light for **1**^{air} (c), and using the 808 nm light for **1**^{air} (d). Colors: **1**^{sol} before irradiation – dark blue; **1**^{sol} after thermal relaxation – pale blue; **1**^{air} before irradiation – yellow; **1**^{air} after thermal relaxation – orange; the $\chi_M T$ curve after irradiation by the 520 nm light – red; the $\chi_M T$ curve after irradiation by the 808 nm light – dark red.

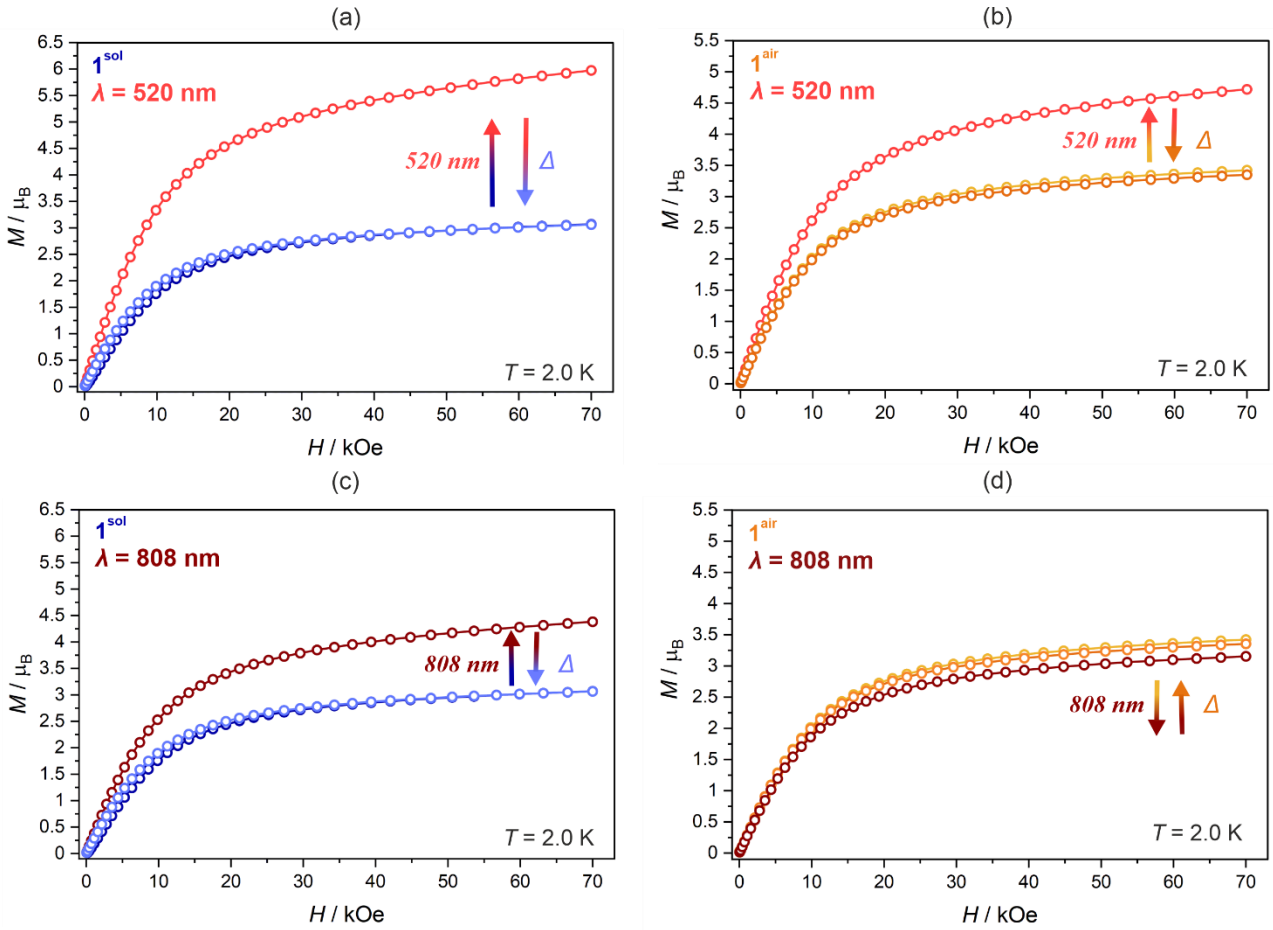

Fig. S19 Magnetization–magnetic field plots before and after irradiation: using the 520 nm light for **1**^{sol} (a), using the 520 nm light for **1**^{air} (b), using the 808 nm light for **1**^{air} (c), and using the 808 nm light for **1**^{air} (d). Colors: **1**^{sol} before irradiation – dark blue; **1**^{sol} after thermal relaxation – pale blue; **1**^{air} before irradiation – yellow; **1**^{air} after thermal relaxation – orange; the *M*(*H*) curve after irradiation by the 520 nm light – pale red; the *M*(*H*) curve after irradiation by the 808 nm light – dark red.

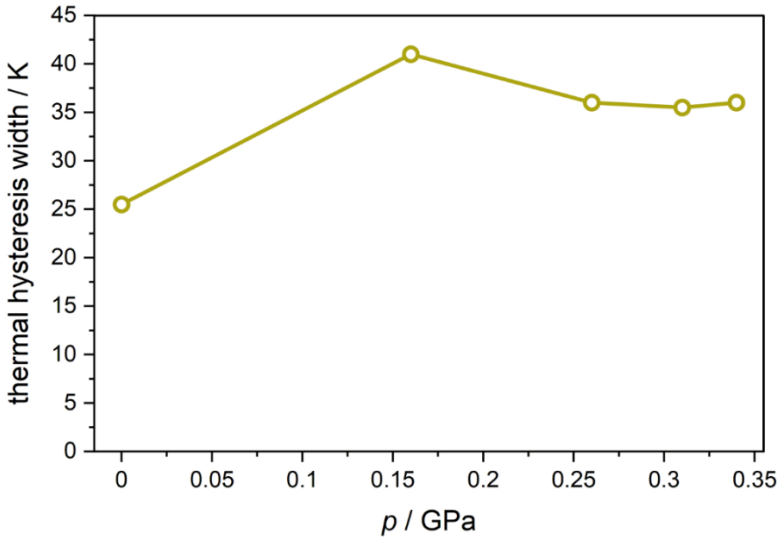

Fig. S20 Correlation between the width of the thermal hysteresis loop of the first (i.e., higher temperature) SCO step in **1**^{air} and the applied external pressure.

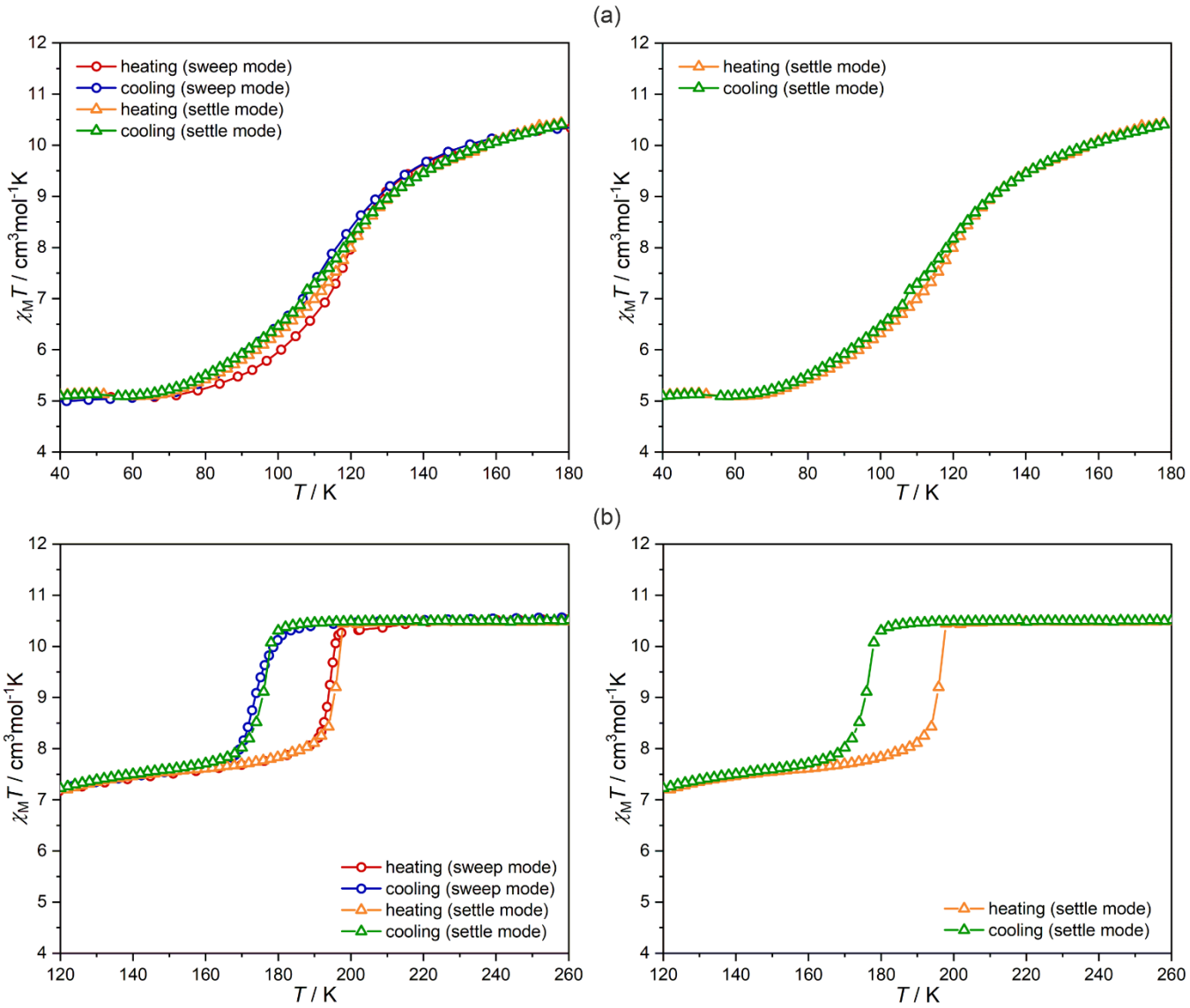

Fig. S21 Comparison of the temperature dependences of the molar magnetic susceptibility–temperature product measured for the sweep mode (labeled as sweep mode, 2 K·min^{-1}, continuous collection of experimental points) and the settle and no-overshoot mode (labeled as settle mode, the experimental points gathered in the 2 K step) for **1**^{sol} (a, left panel) and **1**^{air} (b, left panel), shown for the measurements upon cooling and heating at H_{dc} = 1 kOe, and the respective magnetic curves shown only for the settle mode (right panel; the analogous graphs for the sweep mode only are shown in Fig. 2). Note that here only the representative temperature ranges, corresponding to the largest changes in the magnetic signal with narrow hysteretic behavior in **1**^{sol} and corresponding to the present thermal hysteresis loop in **1**^{air}, are shown. The full temperature ranges are presented in Fig. 2. Note also that the settle mode leads to the narrowing of the thermal hysteresis loop in **1**^{sol} which becomes of a very small width (a) while it does not lead to the distinct change in the much broader thermal hysteresis in **1**^{air} (b, only a tiny thermal shift of the hysteresis can be noted).

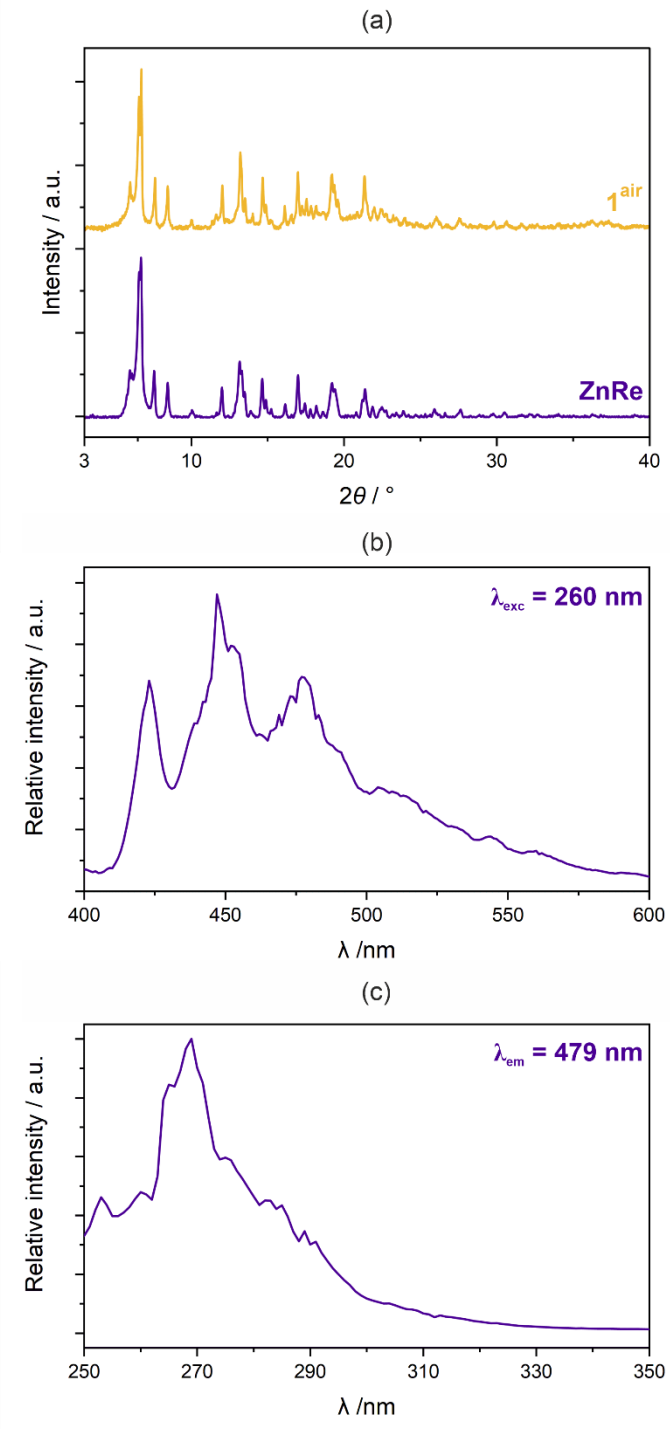

Fig. S22 Powder X-ray diffraction patterns of **1**^{air} and its Zn(II)-containing analog, **ZnRe** (a), the low-temperature (77 K) emission spectrum of **ZnRe** under the indicated excitation (b), and the related excitation spectrum for the emission at 479 nm (c).

Comment to Fig. S22:

The **ZnRe** compound was prepared, for testing the photoluminescence, in the analogous manner as was described for **1**, except for using the zinc(II) perchlorate instead of iron(II) perchlorate (see Experimental section in the main article). The results presented above reveal that the Zn(II)-containing analog of **1**, under drying on the air, is perfectly isostructural with the **1^{air}** phase. Thus, it contains Zn(II) complexes surrounded by cyanido and 4-phpy ligands (Fig. 1). The spectra shown above prove that the ZnRe compound exhibits UV-light-induced blue-green photoluminescence at low temperature (77 K) that can be ascribed to the phosphorescence of 4-phpy ligands.[S6] This emission was too weak at room temperature to be reliably detected with our experimental setup, thus only the low-temperature (i.e., at 77 K) spectra are presented.

We tested the possibility of observing the analogous emission in the case of Fe(II)-containing compound, **1^{air}**, but we did not find any emission signal under any of the UV-to-vis excitation wavelengths neither at room temperature nor low temperature (77 K). This can be explained by simply too weak emission of the 4-phpy ligand at room temperature as it is undetectable even for the Zn(II)-containing analog at room temperature. Therefore, it cannot be observed for **1^{air}** containing the high-spin Fe(II) centers of low-lying excited states as they can further contribute to the emission quenching. We also checked the low-temperature spectra (77 K) but the emission signal was still not observed which is, most probably, due to the strong emission quenching usually observed for the Fe(II) metal centers in their low-spin states that appear at this temperature (Fig. 2).[S7,S8]

We also examined the possibility of observing the emission signal for the mixed Fe(II)–Zn(II) compound (the approximate Fe:Zn molar ratio of 1:1, the sample prepared analogously as **1^{air}** and **ZnRe**) which was the sample that might be emissive with the preservation of at least the partial SCO effect. However, also for this material, we did not observe the photoluminescence at room or low (77 K) temperatures. This can be again related to, in general, the weak photoluminescent ability of 4-phpy ligands as well as the efficient quenching of this emission by Fe(II) centers, even if they occupy the 3d metal sites only partially. This suggests that the organic ligand of more efficient luminescence, e.g., equipped with pyrene or similar emissive substituents,[S7,S8] has to be employed to generate the emission property for the Fe(II)–Re(V) SCO-active materials.

The emission and excitation spectra presented in Fig. S22 were gathered using an FS5 spectrofluorometer (Edinburgh Instruments) containing a Xe (150 W) ac lamp as an excitation source and a Hamamatsu photo-multiplier (R928P type) as a detector. The low-temperature (77 K) spectra were gathered using the optical liquid-nitrogen-cooled dewar and the quartz tube in which the investigated sample was inserted.

References to Supporting Information

S1 M. V. Bennett and J. R. Long, *J. Am. Chem. Soc*., 2003, **125**, 2394–2395.

S2 S. Chorazy, K. Nakabayashi, K. Imoto, J. Mlynarski, B. Sieklucka and S. Ohkoshi, *J. Am. Chem. Soc*., 2012, **134**, 16151–16154.

S3 M. Llunell, D. Casanova, J. Cirera, J. Bofill, P. Alemany, S. Alvarez, M. Pinsky and D. Avnir, *SHAPE v. 2.1. Program for the Calculation of Continuous Shape Measures of Polygonal and Polyhedral Molecular Fragments*, University of Barcelona: Barcelona, Spain, 2013.

S4 D. Casanova, J. Cirera, M. Llunell, P. Alemany, D. Avnir and S. Alvarez, *J. Am. Chem. Soc.*, 2004, **126**, 1755–1763.

S5 S. Alvarez, P. Alemany, D. Casanova, J. Cirera, M. Llunell and D. Avnir, *Coord. Chem. Rev.*, 2005, **249**, 1693–1708.

S6 J. Rzepiela, M. Liberka, M. Zychowicz, J. Wang, H. Tokoro, K. Piotrowska, S. Baś, S. Ohkoshi and S. Chorazy, *Inorg. Chem. Front*., 2024, **11**, 1366–1380.

S7 Y. Jiao, J. Zhu, Y. Guo, W. He and Z. Guo, *New J. Chem*., 2017, **5**, 5214–5222.

S8 B. Benaicha, J. Van Do, A. Yangui, N. Pittala, A. Lusson, M. Sy, G. Bouchez, H. Fourati, C. J. Gomez-Garcia, S. Triki and K. Boukheddaden, *Chem. Sci.*, 2019, **10**, 6791–6798.